THE JOURNAL OF PHYSICAL CHEMISTRY C

Article

Cite This: *J. Phys. Chem. C* 2018, 122, 24499−24511

pubs.acs.org/JPCC

Physical Interpretations of Electrochemical Impedance Spectroscopy of Redox Active Electrodes for Electrical Energy Storage

Bing-Ang Mei,[†] Jonathan Lau,[‡] Terri Lin,[§] Sarah H. Tolbert,[‡,§] Bruce S. Dunn,[‡] and Laurent Pilon*,[†]

[†]Henry Samueli School of Engineering and Applied Science, Mechanical and Aerospace Engineering Department, and [‡]Henry Samueli School of Engineering and Applied Science, Materials Science and Engineering Department, University of California Los Angeles, 420 Westwood Plaza, Los Angeles, California 90095, United States

[§]Department of Chemistry and Biochemistry, University of California Los Angeles, 607 Charles E. Young Drive East, Los Angeles, California 90095, United States

Supporting Information

ABSTRACT: This study aims to provide physical interpretations of electrochemical impedance spectroscopy (EIS) measurements for redox active electrodes in a three-electrode configuration. To do so, a physicochemical transport model was used accounting for (i) reversible redox reactions at the electrode/electrolyte interface, (ii) charge transport in the electrode, (iii) ion intercalation into the pseudocapacitive electrode, (iv) electric double layer formation, and (v) ion electrodiffusion in binary and symmetric electrolytes. Typical Nyquist plots generated by EIS of redox active electrodes were reproduced numerically for a wide range of electrode electrical conductivity, electrolyte thickness, redox reaction rate constant, and bias potential. The electrode, bulk electrolyte, charge transfer, and mass transfer resistances could be unequivocally identified from the Nyquist plots. The electrode and bulk electrolyte resistances were independent of the bias potential, while the sum of the charge and mass transfer resistances increased with increasing bias potential. Finally, these results and interpretation were confirmed experimentally for $LiNi_{0.6}Co_{0.2}Mn_{0.2}O_2$ and MoS_2 electrodes in organic electrolytes.

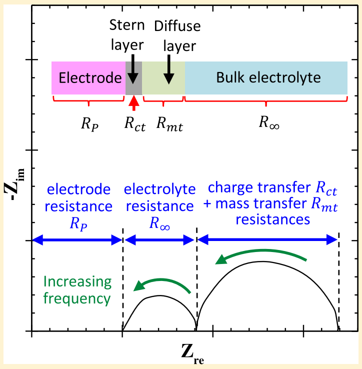

INTRODUCTION

Electrochemical impedance spectroscopy (EIS) has been used to characterize electrodes for batteries,[1−3] electrochemical capacitors,[4−23] dye-sensitized solar cells,[22,24,25] corrosion tests,[26−28] and capacitive deionization.[29,30] It consists of imposing a time harmonic oscillating electric potential $\psi_s(t)$ around a time-independent "dc potential" at the electrode surfaces and measuring the resulting harmonic current density $j_s(t)$.[31−33] The amplitude of the oscillating potential is typically small and less than 10 mV. Using complex notations, the imposed electric potential $\psi_s(t)$ and the resulting current density $j_s(t)$ can be expressed as[31,34−36]

$$\psi_s(t) = \psi_{dc} + \psi_0\, e^{i2\pi ft} \text{ and } j_s(t) = j_{s,dc} + j_{s,0}\, e^{i[2\pi ft - \phi(f)]} \tag{1}$$

where ψ_{dc} is the bias potential, ψ_0 is the amplitude of the oscillating potential at frequency f, $j_{s,dc}$ is the time-independent dc current density, $j_{s,0}$ is the amplitude of the oscillating current density, and $\phi(f)$ is the frequency-dependent phase angle between the imposed potential $\psi_s(t)$ and the current density $j_s(t)$. Then, the electrochemical impedance Z can be defined as[31,34−36]

$$Z = \frac{\psi_s(t) - \psi_{dc}}{j_s(t) - j_{s,dc}} = \frac{\psi_0}{j_{s,0}}\, e^{i\phi} = Z_{re} + iZ_{im} \tag{2}$$

where Z_{re} and Z_{im} (expressed in $\Omega\ m^2$) are the real and imaginary parts of the complex impedance, respectively.

Nyquist plots present the imaginary part $-Z_{im}$ as a function of the real part Z_{re} of the complex impedance. They typically consist of one[7−15] or two[1−3,16−24,28] semicircles at relatively high frequencies and a nonvertical line with respect to the real axis at low frequencies[9−20] for electrodes consisting of transition metal oxides or conductive polymers capable of engaging in reversible redox reactions with ions present in the electrolyte.[15,37−53] Figure 1 shows a typical Nyquist plot for a redox active electrode. It consists of two semicircles, that is, a semicircle at high frequencies between points A and B and one at intermediate frequencies between points B and C, as well as a nonvertical line at low frequencies beyond point C. Note that the nonvertical line may be absent for some redox active electrodes.[1−3,7,8,21−24,28]

Received: May 31, 2018
Revised: August 31, 2018
Published: October 2, 2018

DOI: 10.1021/acs.jpcc.8b05241
J. Phys. Chem. C 2018, 122, 24499−24511

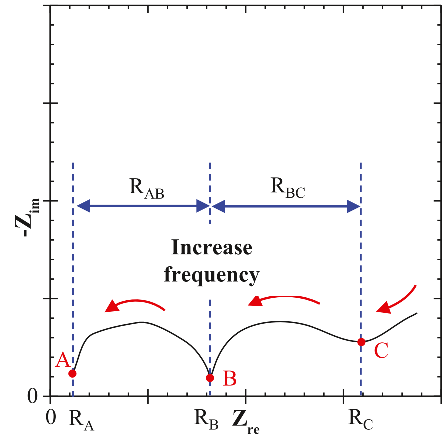

Figure 1. Illustration of typical Nyquist plots obtained for porous $LiNi_{0.6}Co_{0.2}Mn_{0.2}O_2$ pseudocapacitive electrodes in 1 M $LiPF_6$ (EC/DMC) electrolyte with a bias potential ψ_{dc} of 3.7 V.[3]

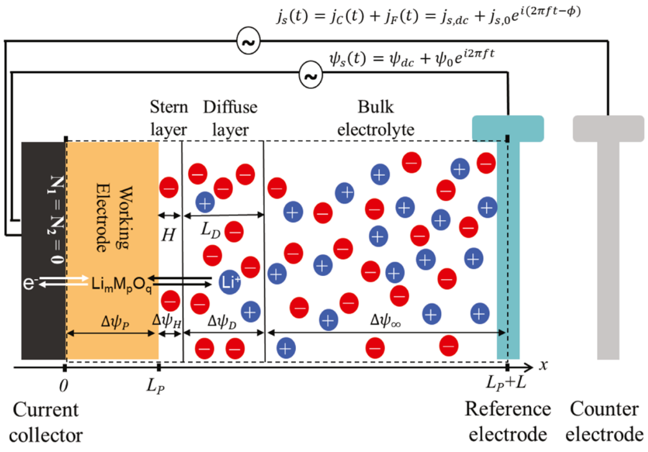

Figure 2. Schematics of the simulated 1D pseudocapacitive electrode in a three-electrode setup. The dashed line encloses the computational domain simulated.

Multiple and often contradictory physical interpretations of experimental Nyquist plots have been proposed in the literature.[7−23] For example, the resistance R_A at point A (Figure 1) has been attributed to (i) the bulk electrolyte resistance[7,11,12,16] or (ii) the sum of the electrode resistance, the bulk electrolyte resistance, and the contact resistance between the electrode and the current collector.[8−10,14,20,22] For Nyquist plots with one semicircle, the diameter of the semicircle has been interpreted as (i) the so-called charge transfer resistance[7,8,11−14] or (ii) the sum of the electrolyte solution and electrode resistances.[15] For Nyquist plots with two semicircles, the diameter of the semicircle at higher frequencies $R_{AB} = R_B - R_A$ (Figure 1) has been assigned to (i) the electrode resistance,[16] (ii) the charge transfer resistance associated with pseudocapacitive charge storage including redox reactions and/or ion intercalation,[17,20,21] or (iii) the electrolyte resistance in the porous electrodes.[18,19,22,23] The diameter of the semicircle at lower frequencies $R_{BC} = R_C - R_B$ (Figure 1) has been attributed to (i) the ionic or so-called diffusion resistance of the electrolyte,[20,21] (ii) the resistance of the solid−electrolyte interphase layer,[1,2] or (iii) the charge transfer resistance.[16−20,22,23] More conservatively, it has also been pointed out that "definitive assignment of each arc to a particular phenomenon is not possible given the probed data".[20] Finally, the nonvertical line beyond point C (Figure 1) at low frequencies (if observed) has been assigned to (i) ion transport limitation in the electrolyte in porous electrode structures[11] or (ii) ion transport limitation in the bulk electrolyte.[16−18]

This study aims to provide a rigorous interpretation of Nyquist plots obtained by EIS for redox active electrodes found in batteries and pseudocapacitors. To do so, EIS measurements of redox active electrodes based on three-electrode configuration were numerically reproduced for a wide range of electrode conductivity, electrolyte thickness, redox reaction rate constant, and bias potential. Then, the physical interpretation of EIS measurements developed numerically was validated experimentally.

■ NUMERICAL ANALYSIS

Schematic and Assumptions. Figure 2 shows a one-dimensional (1D) simulated domain consisting of a planar current collector supporting a planar redox active working electrode of thickness L_P and an electrolyte domain of thickness L corresponding to a three-electrode configuration. Note that our model can also be used to simulate porous electrodes through the use of effective electrical conductivity and ion diffusion coefficient. However, finding the best suited effective medium approximation (EMA) to represent actual porous electrodes falls outside the scope of this study. In addition, EMAs are often for two-phase systems while actual electrodes contain multiple constituents of various shapes and sizes including redox active nanoparticles, binder [e.g., polyvinylidene fluoride (PVDF) and carboxymethylcellulose], and electrical conducting materials [e.g., carbon black, graphene, carbon nanotube (CNT)]. To make the problem mathematically tractable, the following assumptions were made: (1) the electrolyte was binary and symmetric, that is, it consisted of two ion species of opposite valency $\pm z$ ($z > 0$). (2) The two solvated ion species were also assumed to have identical effective diameter a and diffusion coefficient D, as suggested in the literature.[54,55] (3) The stern layer contained no free charge and its thickness H was approximated as the radius of the ions, so that $H = a/2$.[34,56,57] (4) The transport properties of the electrode and electrolyte were taken as constant. (5) Bulk motion of the electrolyte was negligible. (6) Ion intercalation in the electrode was modeled as a diffusion process. (7) Heat generation was ignored and the temperature was uniform and constant in the electrode and electrolyte. (8) The contact resistance between the electrode and the current collector and the resistance of the current collector were negligible. (9) Self-discharge of the electrode was ignored.

Simulations reported in this study for redox active electrodes were based on the modified Poisson−Nernst−Planck (MPNP) model for binary and symmetric electrolyte along with the Frumkin−Butler−Volmer equation for redox reactions.[58,59] The governing equations, initial and boundary conditions, and method of solution were described in detail in refs 59 and 60 and need not be repeated. They are reproduced in Supporting Information for the sake of completeness. The MPNP model [eqs S1−S3] governed the spatiotemporal evolution of the potential $\psi(x,t)$ in the electrode and electrolyte as well as the concentrations $c_1(x,t)$ of cations and $c_2(x,t)$ of anions in the electrolyte. In addition, the concentration $c_{1,P}(x,t)$ of ions intercalated in the electrode was governed by the diffusion equation [eq S4].[60] Moreover, the potential $\psi_s(t)$ at the

DOI: 10.1021/acs.jpcc.8b05241
J. Phys. Chem. C 2018, 122, 24499−24511

current collector/electrode interface was imposed as (i) a harmonic function of time t for EIS simulations [eq S7] and (ii) a triangular function of time t for cyclic voltammetry [eq S8]. The potential and the ion concentrations remained as their initial values at the centerline (Figure 2).

Constitutive Relationships. In order to solve the coupled transient 1D equations as well as the initial and boundary conditions, a total of 21 parameters were necessary including (i) the electrode properties σ_P, k_0, $\Delta\psi_{eq}$, $c_{1,P,max}$, $c_{1,P,0}$, α, and $D_{1,P}$, (ii) the electrolyte properties c_∞, z, ϵ_r, a, and D, (iii) the dimensions of the simulated electrode and electrolyte domains L_P and L, along with (iv) the operating conditions ψ_{dc}, ψ_0, and f for EIS simulations and ψ_{min}, ψ_{max} and v for cyclic voltammetry, and (v) temperature T (in K).

The electrical conductivity σ_P of the electrode, the length of the electrolyte domain L, the redox reaction rate constant k_0, and the bias potential ψ_{dc} were treated as variables to achieve various resistances. Most parameters were taken from the literature. For electrodes consisting of transition metal oxides, the equilibrium potential difference $\Delta\psi_{eq}$ can be modeled as a linear function of the state-of-charge (SOC) defined ad $c_{1,P}/c_{1,P,max}$, where $c_{1,P,max}$ is the maximum intercalated lithium concentration in the pseudocapacitive electrode.[61−63] Note that for 100 μm thick MnO_2 dense films, $\Delta\psi_{eq}(t)$ (in V) was measured as[64]

$$\Delta\psi_{eq}(t) = 10.5[4 - c_{1,P}(t)/c_{1,P,max}] - 39.9 \tag{3}$$

Here, $c_{1,P,max}$ was taken as $c_{1,P,max} \approx 31.9$ mol/L, corresponding to fully lithiated manganese dioxide $LiMnO_2$.[65,66] The initial concentration of Li^+ in the electrode $c_{1,P,0}$ was chosen as the equilibrium concentration solution for electrode potential equal to ψ_{dc}. The transfer coefficient α was assumed to be 0.5. This choice was meant to reduce the parameter space of the problem and to consider the ideal case of identical energy barriers for forward and backward reversible redox reactions.[34] The diffusion coefficient $D_{1,P}$ of the intercalated Li^+ in the transition metal oxides typically ranges from 10^{-16} to 10^{-10} m^2/s.[67] Here, $D_{1,P}$ was chosen as 10^{-14} m^2/s.

As for the electrolyte, we considered 1 M $LiClO_4$ salt in propylene carbonate (PC) solvent such that the bulk ion concentration $c_\infty = 1$ mol/L and valency $z = 1$. The dielectric constant was taken as that of PC, that is, $\epsilon_r = 64.4$.[68] The effective solvated ion diameter a and diffusion coefficient D were taken as those of solvated Li^+ ions in PC such that $a = 0.67$ nm and $D = 2.0 \times 10^{-11}$ m^2/s.[69]

Finally, for EIS simulations, the oscillating potential amplitude was set as $\psi_0 = 5$ mV and the frequency f varied between 0.1 and 8×10^8 Hz. For cyclic voltammetry, the potential window was $\psi_{min} = 0$ V and $\psi_{max} = 0.5$ V and the scan rate v was very low, that is, $v = 0.001$ mV/s, to reproduce conditions with no kinetic limitations. The temperature T was set as $T = 298$ K. Table 1 summarizes the values or ranges of these different input parameters.

Table 1. Value or Range of Electrode and Electrolyte Properties and Dimensions Used in the Simulations Reported in This Study

parameter	symbol	value	unit
electrode conductivity	σ_P	10^{-5} to 5×10^{-4}	S/m
maximum ion concentration in the electrode	$c_{1,P,max}$	31.9	mol/L
initial ion concentration in the electrode	$c_{1,P,0}$	6.38−6.58	mol/L
reaction rate constant	k_0	10^{-9} to 10^{-8}	$m^{1+3\alpha}$ $mol^{-\alpha}$ s^{-1}
transfer coefficient	α	0.5	
diffusion coefficient in the electrode	$D_{1,P}$	10^{-14}	m^2/s
bulk ion concentration	c_∞	1	mol/L
valency	z	1	
dielectric constant	ϵ_r	64.4	
ion diameter	a	0.67	nm
diffusion coefficient in the electrolyte	D	2.0×10^{-11}	m^2/s
electrode thickness	L_P	100	nm
electrolyte thickness	L	16−64	μm
bias potential	ψ_{dc}	0.1−0.6	V
amplitude of oscillating potential	ψ_0	5	mV
frequency	f	0.1 to 5×10^4	Hz
potential window	ψ_{min}	0	V
	ψ_{max}	0.5	V
scan rate	v	0.001	mV/s
temperature	T	298	K

■ DATA PROCESSING

Faradaic and Capacitive Current Densities. The current density at the electrode/electrolyte interface $j_s(t)$ [eq 1] can be expressed as the sum of (i) the capacitive current density $j_C(t)$ resulting from the electric double layer (EDL) formation and (ii) the Faradaic current density $j_F(t)$ related to the redox reactions, that is, $j_s(t) = j_C(t) + j_F(t)$. The capacitive current density $j_C(L_P,t)$ can be defined as[70]

$$j_C(L_P, t) = -\epsilon_0\epsilon_r \frac{\partial^2\psi}{\partial x \partial t}(L_P, t) \tag{4}$$

where $\epsilon_0 = 8.854 \times 10^{-12}$ F/m is the vacuum permittivity. The Faradaic current density $j_F(L_P,t)$ can be defined by the generalized Frumkin−Butler−Volmer model evaluated at the electrode/electrolyte interface and expressed as[34]

$$j_F(L_P, t) = j_{F,ex}(t)\left\{\exp\left[\frac{(1-\alpha)zF\eta(L_P, t)}{R_uT}\right] - \exp\left[\frac{-\alpha zF\eta(L_P, t)}{R_uT}\right]\right\} \tag{5}$$

where $j_{F,ex}(t)$ is the so-called exchange current density, $F = eN_A = 9.648 \times 10^4$ C/mol is the Faraday's constant, and $R_u = 8.314$ J mol^{-1} K^{-1} is the universal gas constant. The exchange current density $j_{F,ex}(t)$ can be written as[71,72]

$$j_{F,ex}(t) = zFk_0[c_1(L_P, t)]^{1-\alpha}[c_{1,P,max} - c_{1,P}(L_P, t)]^{\alpha} [c_{1,P}(L_P, t)]^{\alpha} \tag{6}$$

In addition, the surface overpotential $\eta(L_P,t)$ necessary to drive the redox reactions at the electrode/electrolyte interface can be expressed as[34]

$$\eta(L_P, t) = \Delta\psi_H(t) - \Delta\psi_{eq}(t) \tag{7}$$

where $\Delta\psi_H$ is the potential drop across the stern layer of thickness $H = a/2$ and located between $x = L_P$ and $x = L_P + H$ (Figure 2).

Electrical Resistances. The electrical resistance R_P (in Ω m^2) per unit surface area of the planar electrode and the bulk

DOI: 10.1021/acs.jpcc.8b05241
J. Phys. Chem. C 2018, 122, 24499−24511

Table 2. Simulation Parameters and Corresponding Resistances R_P, R_∞, R_{ct}, and R_{mt} Values for 9 EIS Simulations for Pseudocapacitive Electrodes

case number	σ_P (S/m)	L (μm)	k_0 ($m^{1+3\alpha}$ mol$^{-\alpha}$ s^{-1})	ψ_{dc} (V)	R_P (Ω cm^2)	R_∞ (Ω cm^2)	R_{ct} (Ω cm^2)	R_{mt} (Ω cm^2)
1	1×10^{-4}	64	10^{-9}	0.1	10	4.2	24.3	20.2
2	5×10^{-5}	64	10^{-9}	0.1	20	4.2	13.5	11.4
3	1×10^{-5}	64	10^{-9}	0.1	100	4.2	7.6	6.6
4	5×10^{-5}	32	10^{-9}	0.1	20	2.1	17.1	14.9
5	5×10^{-5}	16	10^{-9}	0.1	20	1.05	19.9	17.7
6	5×10^{-5}	32	5×10^{-9}	0.1	20	2.1	1.4	1.1
7	5×10^{-5}	32	10^{-8}	0.1	20	2.1	0.6	0.5
8	5×10^{-5}	8	10^{-8}	0.1	20	0.53	0.7	0.6
				0.2	20	0.53	0.7	0.6
				0.3	20	0.53	0.8	0.7
				0.4	20	0.53	0.9	0.7
				0.6	20	0.53	1.2	1.0
9	5×10^{-5}	8	0	0.1	20	0.53		
				0.3	20	0.53		
				0.6	20	0.53		

electrolyte resistance R_∞ (in Ω m^2) depend on the thicknesses L_P and L and the electrical conductivities σ_P and σ_∞ of the electrode and electrolyte according to[73,74]

$$R_P = L_P/\sigma_P \tag{8}$$

and

$$R_\infty \approx L/\sigma_\infty \text{ with } \sigma_\infty = (2z^2F^2Dc_\infty)/(R_uT) \tag{9}$$

Moreover, the so-called charge-transfer resistance R_{ct} (in Ω m^2) under EIS simulations can be expressed as[34]

$$R_{ct} = \frac{\eta - \eta_{dc}}{j_F - j_{F,dc}} \tag{10}$$

where η (in V) is the surface overpotential [eq 7], η_{dc} is the time-independent dc overpotential, j_F (in A/m^2) is the resulting Faradaic current density, and $j_{F,dc}$ is the time-independent dc Faradaic current density. Here, η and j_F can also be expressed in complex notation as

$$\eta(t) = \eta_{dc} + \eta_0\, e^{i[2\pi f t - \phi_\eta(f)]} \text{ and}$$

$$j_F(t) = j_{F,dc} + j_{F,0}\, e^{i[2\pi f t - \phi_F(f)]} \tag{11}$$

where η_0 is the amplitude of the oscillating overpotential, $\phi_\eta(f)$ is the frequency-dependent phase angle between the imposed potential $\psi_s(t)$ and the overpotential $\eta(t)$, $j_{F,0}$ is the amplitude of the oscillating Faradaic current density, and $\phi_F(f)$ is the frequency-dependent phase angle between the imposed potential $\psi_s(t)$ and the Faradaic current density $j_F(t)$.

Similarly, the mass-transfer resistance R_{mt} (in Ω m^2) caused by ion transport in the diffuse layer can be expressed as[34]

$$R_{mt} = \frac{\Delta\psi_D - \Delta\psi_{D,dc}}{j_F - j_{F,dc}} \tag{12}$$

where $\Delta\psi_D$ (in V) is the potential drop across the diffuse layer of thickness L_D and located between $x = L_P + H$ and $x = L_P + H + L_D$ (Figure 2), while $\Delta\psi_{D,dc}$ is the time-independent dc potential drop across the diffuse layer. Similarly, using complex notations, $\Delta\psi_D$ can be expressed as

$$\Delta\psi_D = \Delta\psi_{D,dc} + \Delta\psi_{D,0}\, e^{i[2\pi f t - \phi_D(f)]} \tag{13}$$

where $\Delta\psi_{D,0}$ is the amplitude of the oscillating potential drop across the diffuse layer and $\phi_D(f)$ is the frequency-dependent phase angle between the imposed potential $\psi_s(t)$ and the potential drop across the diffuse layer $\Delta\psi_D(t)$.

■ EXPERIMENTAL METHODS

In order to validate experimentally the physical interpretation of EIS obtained numerically, a redox active MoS_2 electrode was synthesized. First, a slurry was prepared by mixing 70 wt % MoS_2 nanoparticles, 10 wt % Super P (Alfa Aesar), 10 wt % multiwall CNTs (mwCNT, Sigma-Aldrich), and 10 wt % PVDF (Kynar) in *N*-methyl-2-pyrrolidinone (Sigma-Aldrich). The MoS_2 nanoparticles were synthesized through the sulfurization of MoO_2 nanoparticles according to a previously reported procedure.[75] Then, the slurry was drop-cast onto a 1 × 1 cm^2 carbon-coated aluminum current collector (MTI) with a weight loading of 0.4 mg MoS_2 nanoparticles. The electrode was dried in air overnight and under vacuum at 120 °C for at least 2 h. Finally, the electrode was placed in a three-neck half-cell with activated carbon counter and (i) Li/Li$^+$ or (ii) Na/Na$^+$ reference electrodes, where each electrode was clipped to and immersed in (i) 1 M $LiClO_4$ (Sigma-Aldrich) in ethylene carbonate/dimethyl carbonate (EC/DMC, 1:1 by volume) or (ii) 1 M $NaClO_4$ (Alfa Aesar) in EC/DMC (1:1 by volume) electrolyte. MoS_2 electrodes were conditioned prior to EIS experiments using a 70 μA current (1C based on the 167 mAh/g theoretical capacity of MoS_2) from 0.8 to 3 V vs Li/Li$^+$ and 0.6 to 2.5 V vs Na/Na$^+$ for 10 cycles to ensure conversion of the MoS_2 from the semiconducting 2H to the semi-metallic 1T phase. EIS measurements were performed on the MoS_2 electrode with a potential amplitude ψ_0 of 10 mV, bias potential ψ_{dc} versus reference electrodes ranging between 1.8 and 2.2 V and frequency f ranging between 0.1 and 2×10^5 Hz. Note that the electrodes were charged/discharged to each bias potential using a low constant current of about 70 μA. In addition, each bias potential was held until the current decayed to half the original value before EIS measurements were performed to ensure that the electrode was at equilibrium.

■ RESULTS AND DISCUSSION

Table 2 summarizes the eight different cases considered to identify the electrode R_P, electrolyte R_∞, charge transfer R_{ct},

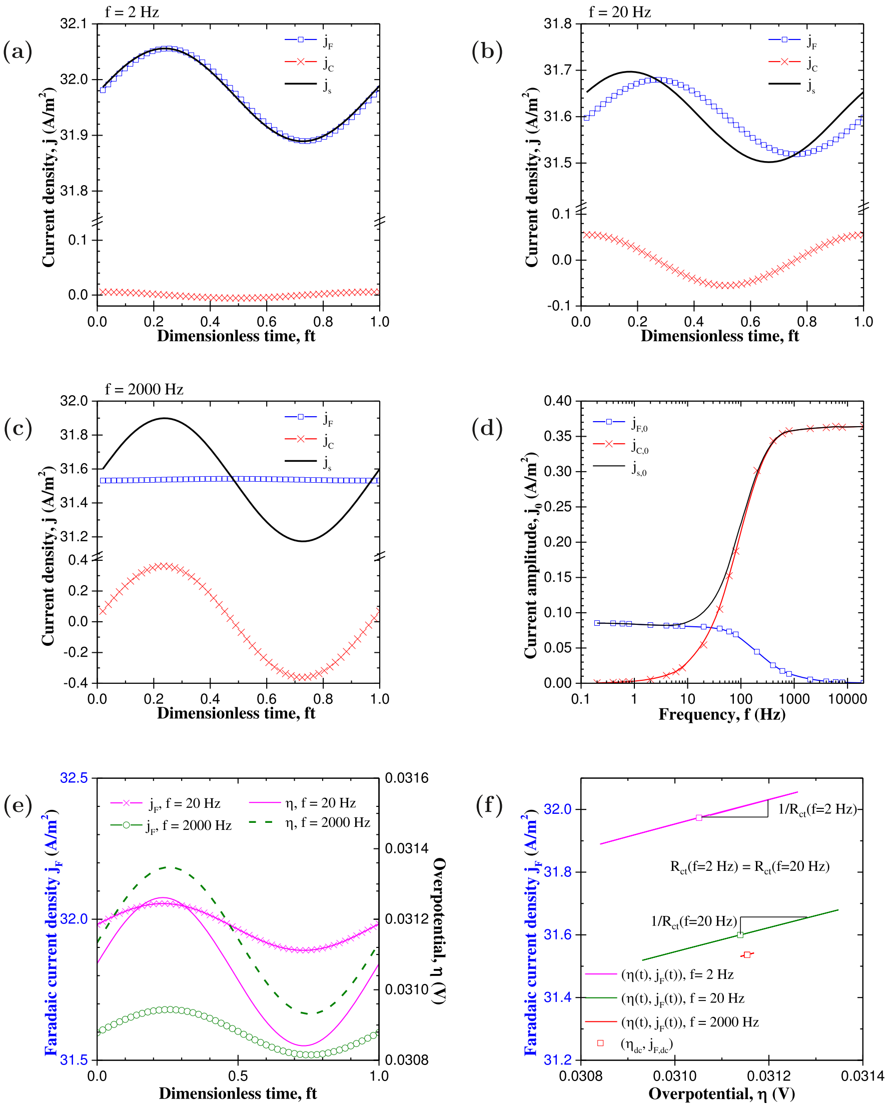

Figure 3. (a−c) Faradaic j_F, capacitive j_C, and total $j_s = j_C + j_F$ current densities as functions of the dimensionless time ft in one oscillating cycle for frequency of (a) 2, (b) 20, and (c) 2000 Hz. (d) Amplitudes of current density oscillations as functions of frequency. (e) Faradaic current density j_F and overpotential η as functions of dimensionless time ft and (f) j_F vs η for frequencies f of 2, 20, and 2000 Hz under EIS simulations.

and mass transfer R_{mt} resistances from the Nyquist plots of redox active electrodes in a three-electrode configuration.

Current Densities and Overpotentials. Figure 3a−c shows the (i) Faradaic current density $j_F(t)$, (ii) capacitive current density $j_C(t)$, and (iii) total current density $j_s(t) = j_C(t) + j_F(t)$ as functions of the dimensionless time ft during one EIS cycle for case 1 (Table 2) at frequency f equal to (a) 2, (b) 20, and (c) 2000 Hz. A phase shift between capacitive and Faradaic current densities was observed at all frequencies. In addition, the Faradaic current density $j_F(t)$ always dominated over the capacitive current density $j_C(t)$ (i.e., $j_{F,dc} > j_{C,dc}$) and their amplitudes were dependent on frequency. Figure 3d shows the amplitudes of oscillations of (i) the Faradaic current density $j_{F,0}$, (ii) the capacitive current density $j_{C,0}$, and (iii) the total current density $j_{s,0}$ as functions of frequency f. It indicates that the amplitude of the Faradaic current density $j_{F,0}$ was the largest at low frequencies while that of the capacitive current density $j_{C,0}$ was the largest at high frequencies. In other words, the major contribution to the impedance Z was the Faradaic reactions at low frequencies and the EDL formation at high frequencies.

Moreover, Figure 3e shows the overpotential $\eta(t)$ and the Faradaic current density $j_F(t)$ as functions of the dimensionless time ft for case 1 (Table 2) at frequency f equal to 2, 20, and 2000 Hz. It indicates that η and j_F were in phase at all frequencies, that is, $\phi_\eta(f) = \phi_F(f)$ [eq 11]. Figure 3f shows j_F as a function of η for EIS simulations for case 1. It established a linear relationship between j_F and η for all frequencies considered. In addition, the amplitude η_0 of the overpotential oscillations were very small. Note that similar conclusions can be drawn from the plot of j_F as a function of $\Delta\psi_D$ (Figure S1 in Supporting Information). Thus, the charge transfer resistance and mass transfer resistance, given by eqs 10 and 12, can be estimated as

$$\frac{1}{R_{ct}} = \frac{j_F(t) - j_{F,dc}}{\eta(t) - \eta_{dc}} \approx \left.\frac{\partial j_F}{\partial \eta}\right|_{\eta=\eta_{dc}} \tag{14}$$

$$\frac{1}{R_{mt}} = \frac{j_F(t) - j_{F,dc}}{\Delta\psi_D(t) - \Delta\psi_{D,dc}} \approx \left.\frac{\partial j_F}{\partial \Delta\psi_D}\right|_{\Delta\psi_D=\Delta\psi_{D,dc}} \tag{15}$$

DOI: 10.1021/acs.jpcc.8b05241
J. Phys. Chem. C 2018, 122, 24499−24511

In other words, $1/R_{ct}$ and $1/R_{mt}$ correspond, respectively, to the slope of j_F versus η and j_F versus $\Delta\psi_D$ near the dc operating points. Figure 3f also indicates that R_{ct} was independent of frequency. Similar observations can be made for the mass transfer resistance R_{mt} [Figure S1b in Supporting Information].

Interpretation of Nyquist Plots. *Electrode Resistance R_P.* Figure 4 shows the Nyquist plots for the electrodes of cases 1−3 featuring electrode electrical conductivity σ_P equal to (a) 1×10^{-4}, (b) 5×10^{-5}, and (c) 1×10^{-5} S/m, corresponding to electrode resistance R_P [eq 8] equal to (a) 10, (b) 20, and (c) 100 Ω cm^2, respectively. All other parameters remained the same in these three cases (Table 2). Note that all values of $-Z_{im}$ simulated were positive for all frequencies. Figure 4 indicates that the high-frequency intersection of the Nyquist plot with the Z_{re}-axis (corresponding to R_A in Figure 1) increased with decreasing conductivity σ_P and was systematically equal to the electrode resistance R_P. Note that the contact resistance was neglected in the current simulations. However, it can be modeled as a resistor in series with the electrode resistance R_P. Its sole effect would be a horizontal shift of the Nyquist plot along the Z_{re}-axis. The same observations have already been made for simulations of electrochemical double layer capacitor (EDLC) electrodes.[73]

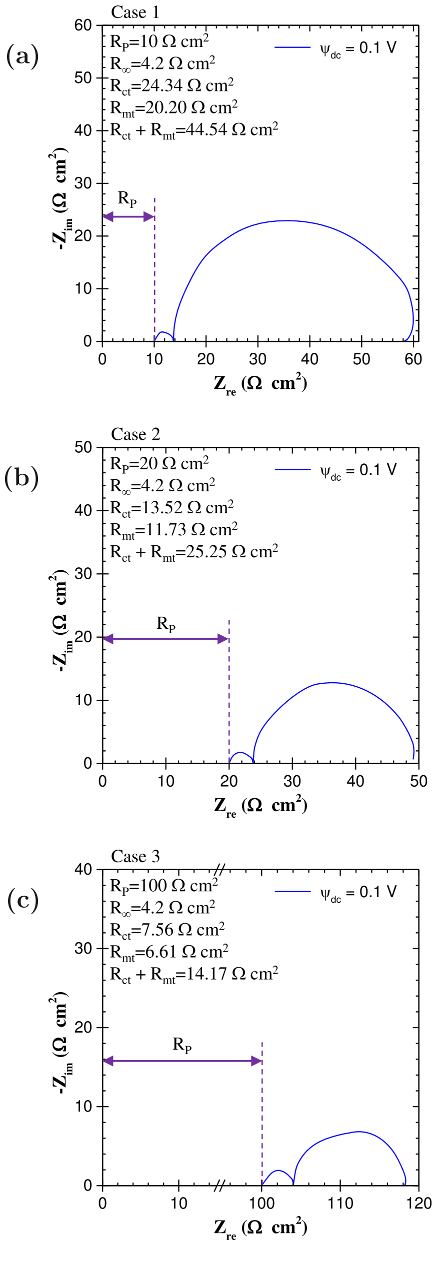

Figure 4. Nyquist plots for redox active electrodes for cases 1−3 featuring electrode resistance R_P equals to (a) 10, (b) 20, and (c) 100 Ω cm^2.

Moreover, the diameter of the semicircle at high frequencies (corresponding to $R_{AB} = R_B - R_A$ in Figure 1) was not affected by the electrode conductivity and was equal to 4.2 Ω cm^2 in all cases. By contrast, the diameter of the semicircle at lower frequencies (corresponding to $R_{BC} = R_C - R_B$ in Figure 1) decreased with decreasing electrode conductivity σ_P.

Bulk Electrolyte Resistance R_∞. Figure 5 shows the Nyquist plots for electrodes of cases 2, 4, and 5 featuring electrolyte

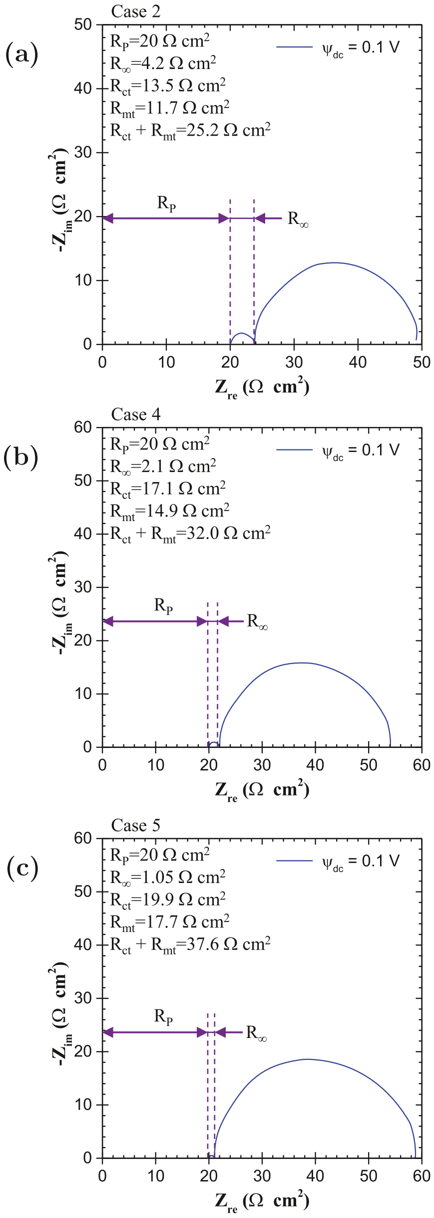

Figure 5. Nyquist plots for redox active electrodes for cases 2, 4, and 5 featuring bulk electrolyte resistance R_∞ equals to (a) 4.2, (b) 2.1, and (c) 1.05 Ω cm^2.

thickness L equal to (a) 64, (b) 32, and (c) 16 μm, corresponding to bulk electrolyte resistance R_∞ [eq 9] equal to (a) 4.2, (b) 2.1, and (c) 1.05 Ω cm^2, respectively. All other parameters remained the same in these three cases. Here, the electrode resistance R_P was constant and equal to 20 Ω cm^2 for all three cases. A previous conclusion identifying $R_A = R_P$ was also valid for these cases. In addition, Figure 5 establishes that the diameter of the semicircle at high frequencies (corresponding to $R_{AB} = R_B - R_A$ in Figure 1) was equal to the bulk electrolyte resistance, that is, $R_{AB} = R_\infty$. In fact, the same observations were made for EDLC electrodes.[73] Moreover, increasing the electrolyte thickness L reduced the diameter of the semicircle at lower frequencies, corresponding to $R_{BC} = R_C - R_B$ (Figure 1).

Charge Transfer R_{ct} and Mass Transfer R_{mt} Resistance. To further explain the diameter of the semicircle at intermediate frequencies (R_{BC} in Figure 1), charge transfer resistance R_{ct} and mass transfer resistance R_{mt} were varied by changing the reaction rate constant k_0. Figure 6 shows the Nyquist plots for electrodes for cases 4, 6, and 7 featuring redox reaction rate constant k_0 equal to (a) 10^{-9}, (b) 5×10^{-9}, and (c) 10^{-8} m$^{2.5}$ mol$^{-0.5}$ s^{-1}. These cases corresponded to charge transfer R_{ct} [eq 10] and mass transfer R_{mt} [eq 12] resistances equal to (a) 24.3 and 20.2 Ω cm^2, (b) 13.5 and 11.7 Ω cm^2, and (c) 7.6 and 6.6 Ω cm^2, respectively. All other parameters remained the same in these three cases. In particular, R_P and R_∞ were equal to 20 and 2.1 Ω cm^2, respectively. Here also, previous identifications of $R_A = R_P$ and $R_{AB} = R_\infty$ remained valid in these cases. Figure 6 establishes that the diameter of the semicircle at lower frequencies R_{BC} (Figure 1) was systematically equal to the sum of charge transfer resistance R_{ct} and mass transfer resistance R_{mt} estimated using eqs 14 and 15, that is, $R_{BC} = R_{ct} + R_{mt}$.

In addition, Figures 4 and 5 indicate that R_{ct} and/or R_{mt} decreased with (i) decreasing electrode conductivity σ_P and (ii) increasing electrolyte thickness L. To explain the trend in R_{ct}, Figure 7a,b shows (i) j_F versus η and j_F versus $\Delta\psi_D$ under cyclic voltammetry at very low scan rate (ν = 0.001 mV/s), where there are no kinetic limitations and (ii) the points (η_{dc}, $j_{F,dc}$) and ($\Delta\psi_{D,dc}$, $j_{F,dc}$) obtained from EIS simulations and averaged from all frequencies considered for different values of (a) σ_P in cases 1−3 and (b) L in cases 2, 4, and 5. The figures indicate that the $j_F-\eta$ curve remained nearly the same for different values of σ_P and L. In addition, the slope of the $j_F-\eta$ curve at (η_{dc}, $j_{F,dc}$), corresponding to $1/R_{ct}$ [eq 14], decreased with increasing dc overpotential η_{dc} which increased with increasing σ_P and decreasing L. Similar observations were made for $j_F-\Delta\psi_D$ curve and $1/R_{mt}$.

To further explain the trend in the overpotential $\eta_{dc} = \Delta\psi_{H,dc} - \Delta\psi_{eq,dc}$ and potential drop across the diffuse layer $\Delta\psi_{D,dc}$, Figure 7c,d shows the dc potential drops across (i) the electrode $\Delta\psi_{P,dc}$, (ii) the stern layer $\Delta\psi_{H,dc}$, (iii) the diffuse layer $\Delta\psi_{D,dc}$, and (iv) the bulk electrolyte $\Delta\psi_{\infty,dc}$ for different values of (c) σ_P in cases 1−3 and (d) L in cases 2, 4, and 5. Note that the imposed dc potential ψ_{dc} at the current collector is such that

$$\psi_{dc} = \Delta\psi_{P,dc} + \Delta\psi_{H,dc} + \Delta\psi_{D,dc} + \Delta\psi_{\infty,dc} \tag{16}$$

Figure 7c indicates that the potential drops $\Delta\psi_{H,dc}$, $\Delta\psi_{D,dc}$, and $\Delta\psi_{\infty,dc}$ increased with increasing σ_P to compensate for the decrease in the potential drop across the electrode $\Delta\psi_{P,dc}$ so as to maintain the imposed ψ_{dc}. Similarly, Figure 7d establishes that the potential drops $\Delta\psi_{P,dc}$, $\Delta\psi_{H,dc}$, and $\Delta\psi_{D,dc}$ decreased with increasing electrolyte thickness L to compensate for the increase in the potential drop across the bulk electrolyte $\Delta\psi_{\infty,dc}$, while ψ_{dc} remained constant. In other words, both potential drops $\Delta\psi_{H,dc}$ and $\Delta\psi_{D,dc}$ increased with increasing σ_P and decreasing L. In addition, under EIS simulations, the variation of SOC of the electrode was negligible, resulting in nearly constant $\Delta\psi_{eq,dc}$. Thus, the dc overpotential $\eta_{dc} = \Delta\psi_{H,dc} - \Delta\psi_{eq,dc}$ and the charge transfer resistance R_{ct} varied like $\Delta\psi_{H,dc}$, that is, they increased with increasing electrical conductivity and decreasing electrolyte thickness L. Note that the potential drop across the diffuse layer $\Delta\psi_{D,dc}$ and the potential drop across the stern layer $\Delta\psi_{H,dc}$ were related[76] (see detailed derivation in Supporting Information). Therefore, the charge transfer resistance R_{ct} [eq 10] and the mass transfer resistance R_{mt} [eq 12] were coupled and could not be separated in the Nyquist plot.

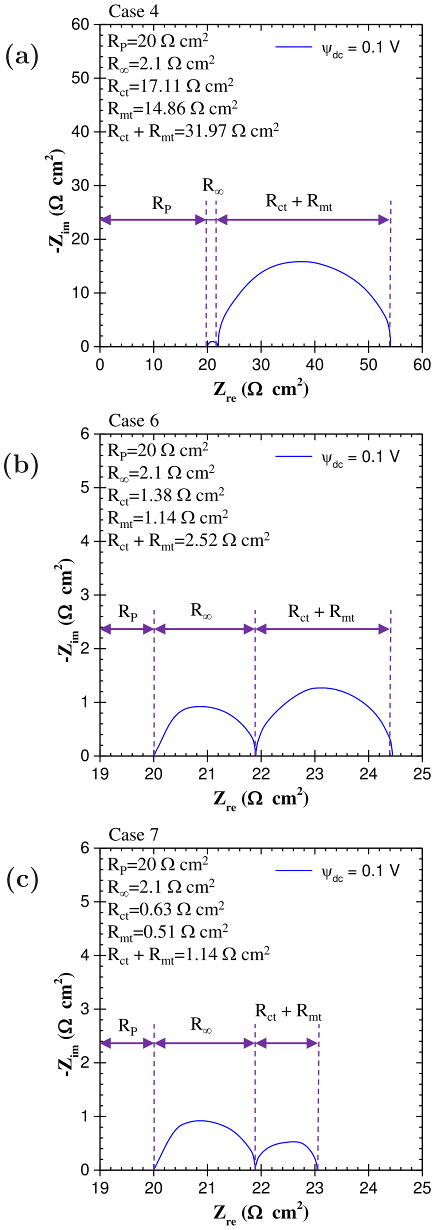

Figure 6. Nyquist plots for redox active electrodes for cases 4, 6, and 7 featuring charge transfer R_{ct} and mass transfer R_{mt} resistances of (a) 24.3 and 20.2 Ω cm^2, (b) 13.5 and 11.7 Ω cm^2, and (c) 7.6 and 6.6 Ω cm^2, respectively.

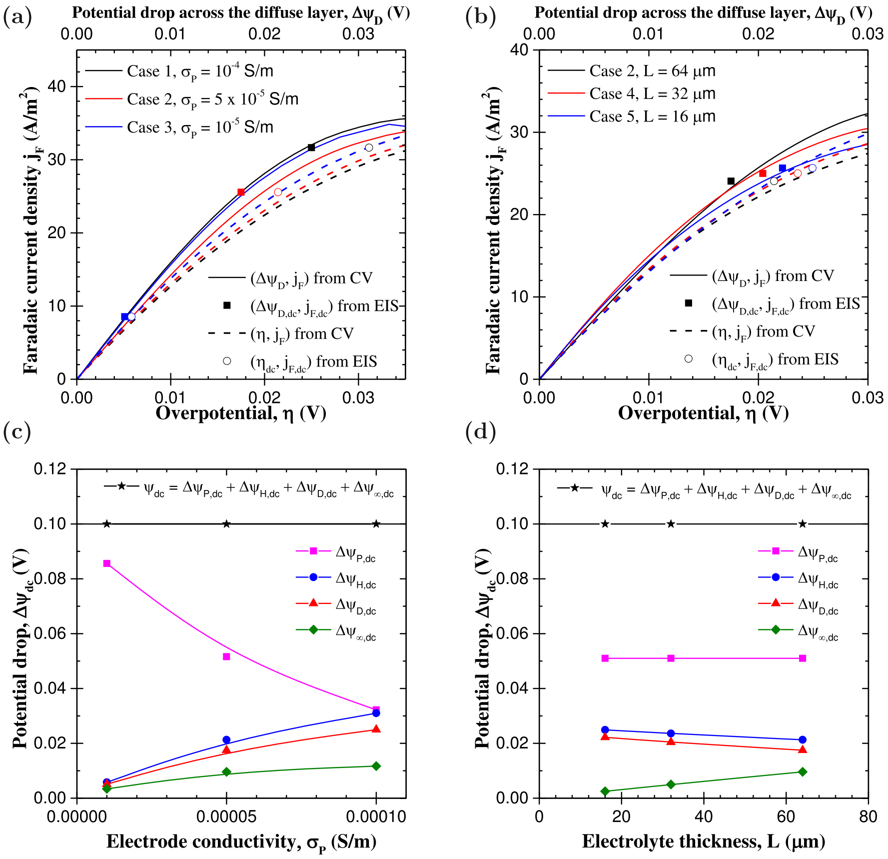

Figure 7. (a,b) Faradaic current j_F as a function of overpotential η and of potential drop across the diffuse layer $\Delta\psi_D$ under cyclic voltammetry at very low scan rate (ν = 0.001 mV/s) as well as (η_{dc}, $j_{F,dc}$) and ($\Delta\psi_{D,dc}$, $j_{F,dc}$) (averaged from all frequencies considered) from EIS simulations and (c,d) dc potential drops from EIS simulations for different values of (a,c) σ_P in cases 1−3 and (b,d) L in cases 2, 4, and 5.

Effect of Bias Potential ψ_{dc}. Figure 8a shows the Nyquist plot for cases 8 and 9 with bias potential ψ_{dc} ranging from 0.1 to 0.6 V. All parameters were identical in cases 8 and 9 except for k_0 equals to $k_0 = 10^{-8}$ m$^{2.5}$ mol$^{-0.5}$ s^{-1} in case 8 (redox active) and $k_0 = 0$ in case 9 (EDLC) (Table 2). Two semicircles were observed for case 8, whereas only one semicircle and a nearly vertical line were observed for case 9. It is important to note that the high frequency semicircle AB for cases 8 and 9 overlapped. In addition, the intercept of the Nyquist plot with the Z_{re} axis (point A) and the semicircle AB at high frequency were independent of ψ_{dc}. Indeed, the resistances of the electrode R_P and bulk electrolyte R_∞ are properties of the electrode and electrolyte. They were both independent of redox reactions and of ψ_{dc}, as indicated in eqs 8 and 9. Moreover, the nearly vertical lines (diffusion tail) observed for case 9 were also nearly independent of dc potential ψ_{dc}, as previously observed for EDLC electrodes.[73] The slope of the line indicated whether the charging process was controlled by EDL formation (large slope) or limited by ion diffusion in the electrolyte (small slope).[73] Here, the slope of the nonvertical line was very steep, indicating that the charging process was controlled by EDL formation in absence of Faradaic reactions.

Furthermore, for case 8, the diameter of the semicircle BC at lower frequency, that is, the charge and/or mass transfer resistances R_{ct} and R_{mt}, increased with increasing ψ_{dc}. Indeed, Figure 8b plots the Faradaic current density j_F versus overpotential η and j_F versus potential drop across the diffuse layer $\Delta\psi_D$ under cyclic voltammetry at very low scan rate (ν = 0.001 mV/s), that is, without kinetic limitations. It also plots the corresponding points (η_{dc}, $j_{F,dc}$) and ($\Delta\psi_{D,dc}$, $j_{F,dc}$) averaged from all frequencies under EIS simulations for the different bias potential ψ_{dc} considered. It indicates that (i) the dc overpotential η_{dc} increased with increasing bias potential ψ_{dc} and (ii) the slope of the j_F−η curve at point (η_{dc}, $j_{F,dc}$), that is, $1/R_{ct}$, decreased with increasing η_{dc}. A similar conclusion can be drawn for $\Delta\psi_D$ and thus for $1/R_{mt}$.

Comparison with Experimental Data. Figure 9a shows the Nyquist plots reported in the literature and obtained experimentally for the $LiNi_{0.6}Co_{0.2}Mn_{0.2}O_2$ electrode in 1 M $LiPF_6$ in EC and ethyl−methyl carbonate (EC/EMC, 3:7) electrolyte for a bias potential ψ_{dc} of 3.7−4.2 V.[3] The experiment was performed in coin-type cells with lithium foil as the counter and reference electrode.[3] Here, the lithium foil electrode was not expected to contribute to the semicircles of the Nyquist plot due to strong redox activity, while the Ohmic resistance of the Li electrode could cause a horizontal shift of the Nyquist plot along the Z_{re}-axis. The Nyquist plots featured two semicircles and closely resembled numerically generated Nyquist plots illustrated in Figure 8a. Note that similar trends were observed in the Nyquist plots obtained for other material systems including corrosion test of SiC composite in sodium hydroxide solution[28] and dye sensitized solar cells.[16,22,24,25] In addition, neither the high-frequency intersection of the Nyquist plot with the Z_{re}-axis R_A nor the diameter of the high frequency semicircle R_{AB} was affected by ψ_{dc}. Similarly, the resistance R_{BC}, interpreted as the charge R_{ct} and/or mass

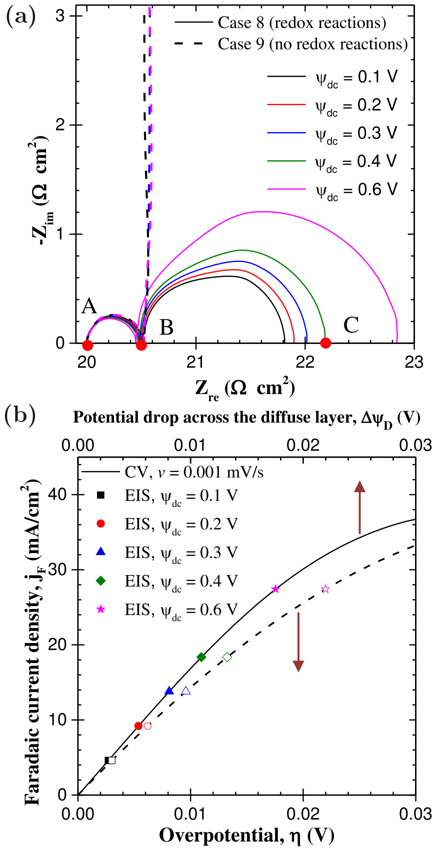

Figure 8. (a) Nyquist plot for cases 8 (redox reactions) and 9 (no redox reactions) with bias potential ψ_{dc} of 0.1−0.6 V. (b) Corresponding Faradaic current density j_F as a function of overpotential η and of potential drop across the diffuse layer $\Delta\psi_D$ under cyclic voltammetry at very low scan rate (ν = 0.001 mV/s) as well as (η_{dc}, $j_{F,dc}$) and ($\Delta\psi_{D,dc}$, $j_{F,dc}$) (averaged from all frequencies considered) from EIS simulations for case 8.

R_{mt} transfer resistances, increased with increasing ψ_{dc}, as also observed in the simulations.

Figure 9b,c shows the Nyquist plots obtained experimentally for MoS_2 mesoporous electrodes in a three-electrode configuration in (b) 1 M $NaClO_4$ (EC/DMC) and (c) 1 M $LiClO_4$ (EC/DMC) electrolytes for bias potential ψ_{dc} ranging between 1.8 and 2.2 V. For both systems, the experimentally measured Nyquist plots feature two partially overlapping (or depressed) semicircles at high frequencies as well as a nonvertical line at low frequencies. The fact that the two semicircles overlapped could be attributed to the fact that ion transport in the electrolyte (corresponding to R_∞) and ion intercalation into the MoS_2 electrode (related to R_{ct} and/or R_{mt}) took place simultaneously throughout the porous electrode. In addition, for both systems, the high-frequency intersection of the Nyquist plot with the Z_{re}-axis (point A) and the high frequency arc AB were not affected by ψ_{dc}. These experimental observations agreed with numerical simulations presented earlier. Moreover, the resistance R_A was identical in both experimental systems. This was consistent with the interpretation that R_A corresponded to the electrode resistance and the fact that both electrodes were nearly identical. In fact, the electrode resistance was equal to 10 Ω and similar to that of activated carbon electrodes (5−10 Ω) of similar dimensions reported in our previous study.[73] On the other hand, the resistance R_{AB} for the system with $NaClO_4$ electrolyte [Figure 9b] was larger than that for $LiClO_4$ electrolyte [Figure 9c]. This was in line with the fact that R_{AB} corresponded to the bulk electrolyte resistance and that $NaClO_4$ in EC/DMC feature lower ionic conductivity (~5 mS/cm)[77] than $LiClO_4$ in EC/DMC (~8.4 mS/cm)[78] at room temperature.

Furthermore, for both systems, the diameter of the second arc BC, that is, the resistance R_{BC}, increased with increasing ψ_{dc}. This was consistent with numerical simulations in the presence of redox reactions (case 8, Figure 8). In addition, for any given bias potential, the resistance R_{BC} for $NaClO_4$ electrolyte was larger than that for $LiClO_4$ electrolyte. Note also that the pseudocapacitive charge storage mechanism for MoS_2 electrode is mainly due to ion intercalation.[79] However, the kinetics of Na^+ intercalation into the MoS_2 electrode was slower than that of Li^+ because of the larger radius and heavier mass of Na^+ compared with Li^+.[79,80] This resulted in larger charge and mass transfer resistances in the $NaClO_4$ than in the $LiClO_4$ electrolyte.

Moreover, the nonvertical line beyond point C could be assigned to ion transport limitation in the electrolyte in the porous electrodes or in the diffuse layer of the EDL. This feature was not observed (i) in numerical simulations for planar redox active electrodes [case 8, Figure 8a] or (ii) in experiments for electrodes made of battery-type $LiNi_{0.6}Co_{0.2}Mn_{0.2}O_2$ material shown in Figure 9a.[3] The latter can be attributed to the dominance of Faradaic reactions at low frequencies (beyond point C). However, a similar nonvertical line was observed in numerically generated Nyquist plots for EDLC electrodes [case 9, Figure 8a], as previously discussed. In fact, by contrast with planar pseudocapacitive electrodes or battery electrodes,[3] the current contribution from EDL formation was likely large in the highly porous MoS_2 electrodes due to the large surface area offered by other constituents of the electrodes (e.g., mwCNTs).

Finally, Figure 9d shows the internal resistance R_{GC} retrieved from the "IR drop" in galvanostatic cycling (see Supporting Information) as a function of the imposed current i_{GC} (1−8 mA) as well as $R_B = R_A + R_{AB}$ retrieved from the Nyquist plots for the two systems considered in Figure 9b,c. It indicates that R_{GC} was nearly independent of the imposed current I_{GC} and was approximately equal to R_B. Note that R_{GC} has been attributed to the Ohmic resistance of the system[81] and is equal to the sum of the electrical resistance of the electrode R_P and the ionic resistance of the electrolyte R_∞.[34,74,81−83] This result confirms the physical interpretation developed from the numerical simulations establishing that $R_B = R_P + R_\infty$.

■ CONCLUSIONS

This study presented physical interpretations of EIS results for redox active electrodes. The Nyquist plots presenting the imaginary and real parts of the complex impedance of individual electrodes were numerically reproduced based on the MPNP model along with the generalized Frumkin−Butler−Volmer equation for redox reactions and closely resembled experimental measurements. This study established that intercepts with the real axis, R_A, R_{AB}, and R_{BC} (shown in Figure 1) can be interpreted as the electrode resistance, the electrolyte resistance, and the sum of charge and mass transfer resistances, respectively. Furthermore, the electrode and bulk electrolyte resistances were independent of the bias potential, while the sum of the charge and mass transfer resistances increased with increasing bias potential. Finally, these results and interpretations were confirmed experimentally for

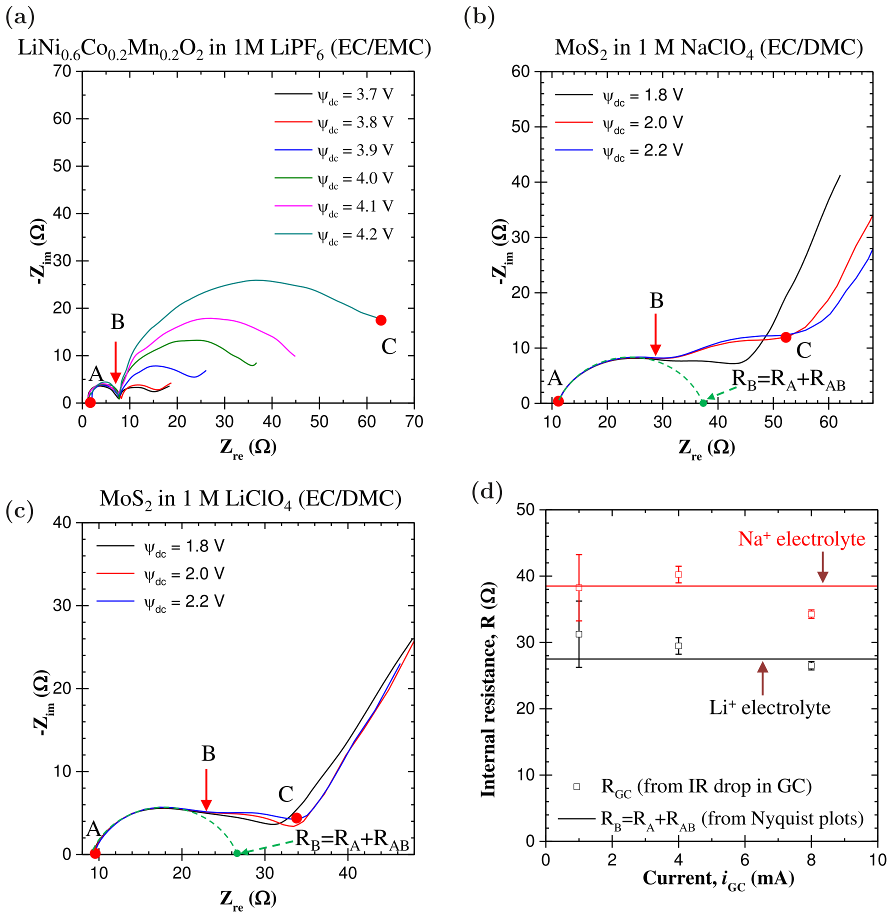

Figure 9. Nyquist plot obtained experimentally for porous electrodes made of (a) $LiNi_{0.6}Co_{0.2}Mn_{0.2}O_2$ in 1 M $LiPF_6$ in EC/EMC(3:7) for bias potential ψ_{dc} of 3.7−4.2 V,[3] (b,c) for MoS_2 mesoporous electrodes in (b) 1 M $NaClO_4$ in EC/DMC and (c) 1 M $LiClO_4$ in EC/DMC for bias potential ψ_{dc} of 1.8−2.2 V. (d) Internal resistance R_{GC} obtained experimentally from galvanostatic cycling as a function of current i_{GC} and R_B obtained from EIS measurement shown in (b,c) for MoS_2 electrodes.

$LiNi_{0.6}Co_{0.2}Mn_{0.2}O_2$ and MoS_2 electrodes in organic electrolytes.

■ ASSOCIATED CONTENT

Supporting Information

The Supporting Information is available free of charge on the ACS Publications website at DOI: 10.1021/acs.jpcc.8b05241.

> Governing equations; initial and boundary conditions of the model; results including current oscillations, potential drops across stern and diffuse layers; and experimental potential evolution under galvanostatic cycling (PDF)

■ AUTHOR INFORMATION

Corresponding Author

*E-mail: pilon@seas.ucla.edu. Phone: +1 (310) 206-5598. Fax: +1 (310) 206-2302.

ORCID

Sarah H. Tolbert: 0000-0001-9969-1582
Bruce S. Dunn: 0000-0001-5669-4740
Laurent Pilon: 0000-0001-9459-8207

Notes

The authors declare no competing financial interest.

■ ACKNOWLEDGMENTS

The computation for this study was performed on the Hoffman2 cluster hosted by the Academic Technology Services (ATS) at the University of California, Los Angeles, USA. This material is also based upon work supported, in part, by the China Scholarship Council (CSC). The partial support of the research by the Office of Naval Research (J.L. and B.D.) is greatly appreciated.

■ NOMENCLATURE

a	effective ion diameter (nm)
c	ion concentration (mol/L)
$c_{1,P}$	concentration of intercalated ion in the pseudocapacitive layer (mol/L)
$c_{1,P,0}$	initial concentration of intercalated ion in the pseudocapacitive layer (mol/L)
$c_{1,P,max}$	maximum concentration of intercalated ion, $c_{1,P,max} = m\rho/M$ (mol/L)
D	diffusion coefficient of ions in electrolyte (m^2/s)
$D_{1,P}$	diffusion coefficient of intercalated ion in the pseudocapacitive electrode (m^2/s)
e	elementary charge, $e = 1.602 \times 10^{-19}$ C
f	frequency (Hz)
F	Faraday's constant, $F = eN_A = 9.648 \times 10^4$ C mol^{-1}
H	stern layer thickness (nm)
i	imaginary unit, $i^2 = -1$

I_s	imposed current (A)
j	current density (A/m^2)
$j_{F,ex}$	exchange current density due to Faradaic reactions (A/m^2)
k_0	reaction rate constant (m$^{2.5}$ mol$^{-0.5}$ s^{-1})
k_B	Boltzmann constant, $k_B = 1.38 \times 10^{-23}$ m^2 kg s^{-2} K^{-1}
L	total thickness of the electrolyte domain (nm)
L_D	thickness of the diffuse layer (nm)
L_P	total thickness of the pseudocapacitive electrode (nm)
n_c	cycle number
N_A	Avogadro number, $N_A = 6.022 \times 10^{23}$ mol^{-1}
N_i	ion flux of species i (mol m^{-2} s^{-1})
R_{ct}	charge transfer resistance (Ω m^2)
R_{mt}	mass transfer resistance (Ω m^2)
R_P	pseudocapacitive electrode resistance (Ω m^2)
R_∞	bulk electrolyte resistance (Ω m^2)
R_u	universal gas constant, $R_u = 8.314$ J mol^{-1} K^{-1}
T	local temperature (K)
t	time (s)
t_{cd}	cycle period for cyclic voltammetry (s)
v	scan rate for cyclic voltammetry (V/s)
z	ion valency
Z	impedance, $Z = Z_{re} + iZ_{im}$ (Ω m^2 or Ω)
Z_{re}, Z_{im}	real and imaginary parts of the impedance (Ω m^2 or Ω)

GREEK SYMBOLS

α, transfer coefficient; ϵ_0, vacuum permittivity, $\epsilon_0 = 8.854 \times 10^{-12}$ F m^{-1}; ϵ_r, dielectric constant of the electrolyte; η, overpotential (V); ν, packing parameter; σ, electrical conductivity (S/m); ϕ, phase difference between ψ_s and j_s (rad); ϕ_D, phase difference between ψ_s and $\Delta\psi_D$ (rad); ϕ_F, phase difference between ψ_s and j_F (rad); ϕ_η, phase difference between ψ_s and η (rad); ψ, electric potential (V); ψ_{min}, ψ_{max}, minimum and maximum of the potential window (V); $\Delta\psi$, potential drop (V); $\Delta\psi_{eq}$, equilibrium potential difference (V)

SUPERSCRIPTS AND SUBSCRIPTS

∞, refers to bulk electrolyte; 0, refers to the amplitude of oscillations; C, refers to the capacitive component; D, refers to diffuse layer; dc, refers to the time-independent dc component; F, refers to the Faradaic component; H, refers to stern layer; i, refers to ion species i; P, refers to pseudocapacitive electrode; s, refers to electrode/current collector interface

REFERENCES

(1) Quan, Z.; Ni, E.; Ogasawara, Y.; Sonoyama, N. Nano-size multiple metal oxide anode electrodes synthesized from layered double hydroxides - Electrochemical reaction mechanism and surface morphology change during reaction with lithium ion. *Solid State Ionics* **2014**, *268*, 268−272.

(2) Li, N.; An, R.; Su, Y.; Wu, F.; Bao, L.; Chen, L.; Zheng, Y.; Shou, H.; Chen, S. The Role of Yttrium Content in Improving Electrochemical Performance of Layered Lithium-Rich Cathode Materials for Li-Ion Batteries. *J. Mater. Chem. A* **2013**, *1*, 9760−9767.

(3) Schipper, F.; Dixit, M.; Kovacheva, D.; Talianker, M.; Haik, O.; Grinblat, J.; Erickson, E. M.; Ghanty, C.; Major, D. T.; Markovsky, B.; et al. Stabilizing Nickel-Rich Layered Cathode Materials by a High-Charge Cation Doping Strategy: Zirconium-Doped LiNi0.6Co0.2Mn0.2O2. *J. Mater. Chem. A* **2016**, *4*, 16073−16084.

(4) Wang, Q.; Yan, J.; Wang, Y.; Wei, T.; Zhang, M.; Jing, X.; Fan, Z. Three-Dimensional Flower-like and Hierarchical Porous Carbon Materials as High-Rate Performance Electrodes for Supercapacitors. *Carbon* **2014**, *67*, 119−127.

(5) Farma, R.; Deraman, M.; Awitdrus, A.; Talib, I. A.; Taer, E.; Basri, N. H.; Manjunatha, J. G.; Ishak, M. M.; Dollah, B. N. M.; Hashmi, S. A. Preparation of Highly Porous Binderless Activated Carbon Electrodes from Fibres of Oil Palm Empty Fruit Bunches for Application in Supercapacitors. *Bioresour. Technol.* **2013**, *132*, 254−261.

(6) Inal, I. I. G.; Holmes, S. M.; Banford, A.; Aktas, Z. the Performance of Supercapacitor Electrodes Developed from Chemically Activated Carbon Produced from Waste Tea. *Appl. Surf. Sci.* **2015**, *357*, 696−703.

(7) Han, G.-Q.; Liu, Y.-R.; Hu, W.-H.; Dong, B.; Li, X.; Shang, X.; Chai, Y.-M.; Liu, Y.-Q.; Liu, C.-G. Crystallographic Structure and Morphology Transformation of MnO2 Nanorods as Efficient Electrocatalysts for Oxygen Evolution Reaction. *J. Electroanal. Chem.* **2016**, *163*, H67−H73.

(8) Jin, P.; Zhang, X.; Zhen, M.; Wang, J. MnO2 Nanotubes with Graphene-Assistance as Low-Cost Counter-Electrode Materials in Dye-Sensitized Solar Cells. *RSC Adv.* **2016**, *6*, 10938−10942.

(9) He, Y.; Chen, W.; Li, X.; Zhang, Z.; Fu, J.; Zhao, C.; Xie, E. Freestanding Three-Dimensional Graphene/MnO2 Composite Networks as Ultralight and Flexible Supercapacitor Electrodes. *ACS Nano* **2012**, *7*, 174−182.

(10) Vidhyadharan, B.; Misnon, I. I.; Aziz, R. A.; Padmasree, K. P.; Yusoff, M. M.; Jose, R. Superior Supercapacitive Performance in Electrospun Copper Oxide Nanowire Electrodes. *J. Mater. Chem. A* **2014**, *2*, 6578−6588.

(11) Huang, Y.; Li, Y.; Hu, Z.; Wei, G.; Guo, J.; Liu, J. A Carbon Modified MnO2 Nanosheet Array as a Stable High-Capacitance Supercapacitor Electrode. *J. Mater. Chem. A* **2013**, *1*, 9809−9813.

(12) Krishnamoorthy, K.; Veerasubramani, G. K.; Pazhamalai, P.; Kim, S. J. Designing Two Dimensional Nanoarchitectured MoS2 Sheets Grown on Mo Foil as a Binder Free Electrode for Supercapacitors. *Electrochim. Acta* **2016**, *190*, 305−312.

(13) Qu, Q.; Zhang, P.; Wang, B.; Chen, Y.; Tian, S.; Wu, Y.; Holze, R. Electrochemical Performance of MnO2 Nanorods in Neutral Aqueous Electrolytes as a Cathode for Asymmetric Supercapacitors. *J. Phys. Chem. C* **2009**, *113*, 14020−14027.

(14) Sankar, K. V.; Selvan, R. K. The Preparation of MnFe2O4 Decorated Flexible Graphene Wrapped with PANI and Its Electrochemical Performances for Hybrid Supercapacitors. *RSC Adv.* **2014**, *4*, 17555−17566.

(15) Subramanian, V.; Zhu, H.; Wei, B. Synthesis and Electrochemical Characterizations of Amorphous Manganese Oxide and Single Walled Carbon Nanotube Composites as Supercapacitor Electrode Materials. *Electrochem. Commun.* **2006**, *8*, 827−832.

(16) Maheswari, D.; Venkatachalam, P. Enhanced Performance of Bi-Layer Nb2O5 Coated TiO2 Nanoparticles/Nanowires Composite Photoanode in Dye-Sensitized Solar Cells. *Photonics Nanostruct. Fund. Appl.* **2014**, *12*, 515−526.

(17) Meher, S. K.; Justin, P.; Ranga Rao, G. Nanoscale Morphology Dependent Pseudocapacitance of NiO: Influence of Intercalating Anions during Synthesis. *Nanoscale* **2011**, *3*, 683−692.

(18) Pang, Q.; Zhao, Y.; Bian, X.; Ju, Y.; Wang, X.; Wei, Y.; Liu, B.; Du, F.; Wang, C.; Chen, G. Hybrid graphene@MoS2@TiO2 microspheres for use as a high performance negative electrode material for lithium ion batteries. *J. Mater. Chem. A* **2017**, *5*, 3667−3674.

(19) Sahu, T. S.; Mitra, S. Exfoliated MoS2 Sheets and Reduced Graphene Oxide-an Excellent and Fast Anode for Sodium-ion Battery. *Sci. Rep.* **2015**, *5*, 12571.

(20) Wang, S.; Hsia, B.; Carraro, C.; Maboudian, R. High-Performance All Solid-state Micro-supercapacitor Based on Patterned Photoresist-derived Porous Carbon Electrodes and an Ionogel Electrolyte. *J. Mater. Chem. A* **2014**, *2*, 7997−8002.

(21) Thangappan, R.; Kalaiselvam, S.; Elayaperumal, A.; Jayavel, R.; Arivanandhan, M.; Karthikeyan, R.; Hayakawa, Y. Graphene Decorated with MoS2 Nanosheets: a Synergetic Energy Storage

Composite Electrode for Supercapacitor Applications. *Dalton Trans.* **2016**, *45*, 2637−2646.

(22) Xiao, Y.; Han, G.; Zhou, H.; Li, Y.; Lin, J.-Y. Nickel Sulfide Counter Electrodes Enhanced by Hydrosulphuric Acid Hydrothermal Treatments for Use in Pt-Free Dye-Sensitized Solar Cells. *Electrochim. Acta* **2015**, *155*, 103−109.

(23) Ye, Z.-G.; Meng, H.-M.; Sun, D.-B. Electrochemical impedance spectroscopic (EIS) investigation of the oxygen evolution reaction mechanism of Ti/IrO2+MnO2 electrodes in 0.5m H2SO4 solution. *J. Electroanal. Chem.* **2008**, *621*, 49−54.

(24) Lin, C.-H.; Tsai, C.-H.; Tseng, F.-G.; Ma, C.-C. M.; Wu, H.-C.; Hsieh, C.-K. Three-Dimensional Vertically Aligned Hybrid Nanoarchitecture of Two-Dimensional Molybdenum Disulfide Nanosheets Anchored on Directly Grown One-Dimensional Carbon Nanotubes for Use as a Counter Electrode in Dye-Sensitized Solar Cells. *J. Alloys Compd.* **2017**, *692*, 941−949.

(25) Xiao, Y.; Wu, J.; Lin, J.-Y.; Tai, S.-Y.; Yue, G. Pulse Electrodeposition of CoS on MWCNT/Ti as a High Performance Counter Electrode for a Pt-Free Dye-Sensitized Solar Cell. *J. Mater. Chem. A* **2013**, *1*, 1289−1295.

(26) Li, W.; He, Q.; Pei, C.; Hou, B. Experimental and Theoretical Investigation of the Adsorption Behaviour of New Triazole Derivatives as Inhibitors for Mild Steel Corrosion in Acid Media. *Electrochim. Acta* **2007**, *52*, 6386−6394.

(27) Maocheng, Y. A. N.; Jin, X. U.; Libao, Y. U.; Tangqing, W. U.; Cheng, S. U. N.; Wei, K. E. EIS Analysis on Stress Corrosion Initiation of Pipeline Steel under Disbonded Coating in Near-Neutral pH Simulated Soil Electrolyte. *Corros. Sci.* **2016**, *110*, 23−34.

(28) Reena Kumari, P. R.; Nayak, J.; Nityananda Shetty, A. N. Corrosion Behavior of 6061/Al-15 vol. pct. SiC (p) Composite and the Base Alloy in Sodium Hydroxide Solution. *Arabian J. Chem.* **2016**, *9*, S1144−S1154.

(29) Wang, H.; Shi, L.; Yan, T.; Zhang, J.; Zhong, Q.; Zhang, D. Design of Graphene-Coated Hollow Mesoporous Carbon Spheres as High Performance Electrodes for Capacitive Deionization. *J. Mater. Chem. A* **2014**, *2*, 4739−4750.

(30) Wang, H.; Zhang, D.; Yan, T.; Wen, X.; Zhang, J.; Shi, L.; Zhong, Q. Three-Dimensional Macroporous Graphene Architectures as High Performance Electrodes for Capacitive Deionization. *J. Mater. Chem. A* **2013**, *1*, 11778−11789.

(31) Yuan, X. Z.; Song, C.; Wang, H.; Zhang, J. *Electrochemical Impedance Spectroscopy in PEM Fuel Cells: Fundamentals and Applications*; Springer-Verlag: London, UK, 2010.

(32) Pech, D.; Brunet, M.; Durou, H.; Huang, P.; Mochalin, V.; Gogotsi, Y.; Taberna, P.-L.; Simon, P. Ultrahigh-Power Micrometre-Sized Supercapacitors Based on Onion-like Carbon. *Nat. Nanotechnol.* **2010**, *5*, 651−654.

(33) Itoi, H.; Nishihara, H.; Kogure, T.; Kyotani, T. Three-Dimensionally Arrayed and Mutually Connected 1.2-nm Nanopores for High-Performance Electric Double Layer Capacitor. *J. Am. Chem. Soc.* **2011**, *133*, 1165−1167.

(34) Bard, A. J.; Faulkner, L. R.; Leddy, J.; Zoski, C. G. *Electrochemical Methods: Fundamentals and Applications*; John Wiley & Sons: Hoboken, NJ, 1980; Vol. 2.

(35) Lasia, A. In *Modern Aspects of Electrochemistry*; Conway, B. E., Bockris, J. O. M., White, R. E., Eds.; Kluwer Academic Publishers: New York, NY, 2002; Chapter 2, No. 32, pp 143−248.

(36) Orazem, M. E.; Tribollet, B. *Electrochemical Impedance Spectroscopy*; John Wiley & Sons: Hoboken, NJ, 2008.

(37) Halper, M. S.; Ellenbogen, J. C. *Supercapacitors: A Brief Overview*. Report No. MP 05W0000272; The MITRE Corporation, McLean, VA, 2006.

(38) Augustyn, V.; Simon, P.; Dunn, B. Pseudocapacitive Oxide Materials for High-Rate Electrochemical Energy Storage. *Energy Environ. Sci.* **2014**, *7*, 1597−1614.

(39) Wei, W.; Cui, X.; Chen, W.; Ivey, D. G. Manganese Oxide-Based Materials as Electrochemical Supercapacitor Electrodes. *Chem. Soc. Rev.* **2011**, *40*, 1697−1721.

(40) Zhang, Y.; Feng, H.; Wu, X.; Wang, L.; Zhang, A.; Xia, T.; Dong, H.; Li, X.; Zhang, L. Progress of Electrochemical Capacitor Electrode Materials: A Review. *Int. J. Hydrogen Energy* **2009**, *34*, 4889−4899.

(41) Li, Q.; Lu, X.-F.; Xu, H.; Tong, Y.-X.; Li, G.-R. Carbon/MnO2 Double-Walled Nanotube Arrays with Fast Ion and Electron Transmission for High-Performance Supercapacitors. *ACS Appl. Mater. Interfaces* **2014**, *6*, 2726−2733.

(42) Fan, Z.; Chen, J.; Wang, M.; Cui, K.; Zhou, H.; Kuang, Y. Preparation and Characterization of Manganese Oxide/CNT Composites as Supercapacitive Materials. *Diamond Relat. Mater.* **2006**, *15*, 1478−1483.

(43) Lee, S. W.; Kim, J.; Chen, S.; Hammond, P. T.; Shao-Horn, Y. Carbon Nanotube/Manganese Oxide Ultrathin Film Electrodes for Electrochemical Capacitors. *ACS Nano* **2010**, *4*, 3889−3896.

(44) Lee, C. Y.; Tsai, H. M.; Chuang, H. J.; Li, S. Y.; Lin, P.; Tseng, T. Y. Characteristics and Electrochemical Performance of Supercapacitors with Manganese Oxide-Carbon Nanotube Nanocomposite Electrodes. *J. Electrochem. Soc.* **2005**, *152*, A716−A720.

(45) Yan, J.; Fan, Z.; Wei, T.; Qian, W.; Zhang, M.; Wei, F. Fast and Reversible Surface Redox Reaction of Graphene−MnO2 Composites as Supercapacitor Electrodes. *Carbon* **2010**, *48*, 3825−3833.

(46) Fischer, A. E.; Pettigrew, K. A.; Rolison, D. R.; Stroud, R. M.; Long, J. W. Incorporation of Homogeneous, Nanoscale MnO2 within Ultraporous Carbon Structures via Self-Limiting Electroless Deposition: Implications for Electrochemical Capacitors. *Nano Lett.* **2007**, *7*, 281−286.

(47) Zhou, H.; Wang, X.; Sheridan, E.; Gao, H.; Du, J.; Yang, J.; Chen, D. Boosting the Energy Density of 3D Dual-Manganese Oxides-Based Li-Ion Supercabattery by Controlled Mass Ratio and Charge Injection. *J. Electrochem. Soc.* **2016**, *163*, A2618−A2622.

(48) Lee, J. W.; Hall, A. S.; Kim, J.-D.; Mallouk, T. E. A Facile and Template-Free Hydrothermal Synthesis of Mn3O4 Nanorods on Graphene Sheets for Supercapacitor Electrodes with Long Cycle Stability. *Chem. Mater.* **2012**, *24*, 1158−1164.

(49) Chen, Y.; Liu, C. G.; Liu, C.; Lu, G. Q.; Cheng, H. M. Growth of single-crystal α-MnO2 nanorods on multi-walled carbon nanotubes. *Mater. Res. Bull.* **2007**, *42*, 1935−1941.

(50) Wang, G.-X.; Zhang, B.-L.; Yu, Z.-L.; Qu, M.-Z. Manganese Oxide/MWNTs Composite Electrodes for Supercapacitors. *Solid State Ionics* **2005**, *176*, 1169−1174.

(51) Raymundo-Piñero, E.; Khomenko, V.; Frackowiak, E.; Béguin, F. Performance of Manganese Oxide/CNTs Composites as Electrode Materials for Electrochemical Capacitors. *J. Electrochem. Soc.* **2005**, *152*, A229−A235.

(52) Xiao, J.; Wan, L.; Yang, S.; Xiao, F.; Wang, S. Design Hierarchical Electrodes with Highly Conductive NiCo2S4 Nanotube Arrays Grown on Carbon Fiber Paper for High-Performance Pseudocapacitors. *Nano Lett.* **2014**, *14*, 831−838.

(53) Wan, L.; Xiao, J.; Xiao, F.; Wang, S. Nanostructured (Co, Ni)-Based Compounds Coated on a Highly Conductive Three Dimensional Hollow Carbon Nanorod Array (HCNA) Scaffold for High Performance Pseudocapacitors. *ACS Appl. Mater. Interfaces* **2014**, *6*, 7735−7742.

(54) Bazant, M. Z.; Kilic, M. S.; Storey, B. D.; Ajdari, A. Towards an Understanding of induced-Charge Electrokinetics at Large Applied Voltages in Concentrated Solutions. *Adv. Colloid Interface Sci.* **2009**, *152*, 48−88.

(55) Qiao, R.; Aluru, N. R. Ion Concentrations and Velocity Profiles in Nanochannel Electroosmotic Flows. *J. Chem. Phys.* **2003**, *118*, 4692−4701.

(56) Wang, H.; Thiele, A.; Pilon, L. Simulations of Cyclic Voltammetry for Electric Double Layers in Asymmetric Electrolytes: A Generalized Modified Poisson-Nernst-Planck Model. *J. Phys. Chem. C* **2013**, *117*, 18286−18297.

(57) Masliyah, J. H.; Bhattacharjee, S. *Electrokinetic and Colloid Transport Phenomena*; John Wiley & Sons: Hoboken, NJ, 2006.

(58) Bazant, M. Z.; Thornton, K.; Ajdari, A. Diffuse-Charge Dynamics in Electrochemical Systems. *Phys. Rev. E: Stat., Nonlinear, Soft Matter Phys.* **2004**, *70*, 021506.

(59) Wang, H.; Pilon, L. Intrinsic Limitations of Impedance Measurements in Determining Electric Double Layer Capacitances. *Electrochim. Acta* **2012**, *63*, 55−63.

(60) Girard, H.-L.; Wang, H.; d'Entremont, A.; Pilon, L. Physical Interpretation of Cyclic Voltammetry for Hybrid Pseudocapacitors. *J. Phys. Chem. C* **2015**, *119*, 11349−11361.

(61) Jow, T. R.; Zheng, J. P. Electrochemical Capacitors using Hydrous Ruthenium Oxide and Hydrogen Inserted Ruthenium Oxide. *J. Electrochem. Soc.* **1998**, *145*, 49−52.

(62) Sikha, G.; White, R. E.; Popov, B. N. A Mathematical Model for a Lithium-Ion Battery/Electrochemical Capacitor Hybrid System. *J. Electrochem. Soc.* **2005**, *152*, A1682.

(63) Kim, H.; Popov, B. N. A Mathematical Model of Oxide, Carbon Composite Electrode for Supercapacitors. *J. Electrochem. Soc.* **2003**, *150*, A1153.

(64) Guillemet, P.; Brousse, T.; Crosnier, O.; Dandeville, Y.; Athouel, L.; Scudeller, Y. Modeling pseudo capacitance of manganese dioxide. *Electrochim. Acta* **2012**, *67*, 41−49.

(65) Zhong, Q.; Huang, B.; Ma, J.; Li, H. Experimental Study on Relationship between SOC and OCV of Lithium-Ion Batteries. *Int. J. Smart Grid Clean Energy* **2014**, *3*, 149−153.

(66) Mei, B.-A.; Li, B.; Lin, J.; Pilon, L. Multidimensional Cyclic Voltammetry Simulations of Pseudocapacitive Electrodes with a Conducting Nanorod Scaffold. *J. Electrochem. Soc.* **2017**, *164*, A3237−A3252.

(67) Colclasure, A. M.; Kee, R. J. Thermodynamically Consistent Modeling of Elementary Electrochemistry in Lithium-Ion Batteries. *Electrochim. Acta* **2010**, *55*, 8960−8973.

(68) Janz, G. J.; Tomkins, R. P. T. *Nonaqueous Electrolytes Handbook*; Academic Press: New York, NY, 1972; Vol. *I*.

(69) Nishikawa, K.; Fukunaka, Y.; Sakka, T.; Ogata, Y. H.; Selman, J. R. Measurement of LiClO4 Diffusion Coefficient in Propylene Carbonate by Moiré Pattern. *J. Electrochem. Soc.* **2006**, *153*, A830−A834.

(70) Cohen, H.; Cooley, J. W. The Numerical Solution of the Time-Dependent Nernst-Planck Equations. *Biophys. J.* **1965**, *5*, 145−162.

(71) Subramanian, V. R.; Boovaragavan, V.; Ramadesigan, V.; Arabandi, M. Mathematical Model Reformulation for Lithium-Ion Battery Simulations: Galvanostatic Boundary Conditions. *J. Electrochem. Soc.* **2009**, *156*, A260−A271.

(72) Goldin, G. M.; Colclasure, A. M.; Wiedemann, A. H.; Kee, R. J. Three-Dimensional Particle-Resolved Models of Li-Ion Batteries to Assist the Evaluation of Empirical Parameters in One-Dimensional Models. *Electrochim. Acta* **2012**, *64*, 118−129.

(73) Mei, B.-A.; Munteshari, O.; Lau, J.; Dunn, B.; Pilon, L. Physical Interpretations of Nyquist Plots for EDLC Electrodes and Devices. *J. Phys. Chem. C* **2017**, *122*, 194−206.

(74) Conway, B. E. *Electrochemical Supercapacitors: Scientific Fundamentals and Technological Applications*; Kluwer Academic/Plenum Publishers: New York, NY, 1999.

(75) Cook, J. B.; Kim, H.-S.; Lin, T. C.; Lai, C.-H.; Dunn, B.; Tolbert, S. H. Pseudocapacitive Charge Storage in Thick Composite MoS2 Nanocrystal-Based Electrodes. *Adv. Energy Mater.* **2017**, *7*, 1601283.

(76) Wang, H.; Fang, J.; Pilon, L. Scaling laws for carbon-based electric double layer capacitors. *Electrochim. Acta* **2013**, *109*, 316−321.

(77) Bhide, A.; Hofmann, J.; Katharina Dürr, A.; Janek, J.; Adelhelm, P. Electrochemical stability of non-aqueous electrolytes for sodium-ion batteries and their compatibility with Na0.7CoO2. *Phys. Chem. Chem. Phys.* **2014**, *16*, 1987−1998.

(78) Xu, K. Nonaqueous Liquid Electrolytes for Lithium-Based Rechargeable Batteries. *Chem. Rev.* **2004**, *104*, 4303−4418.

(79) Cook, J. B.; Kim, H.-S.; Yan, Y.; Ko, J. S.; Robbennolt, S.; Dunn, B.; Tolbert, S. H. Mesoporous MoS2 as a Transition Metal Dichalcogenide Exhibiting Pseudocapacitive Li and Na-Ion Charge Storage. *Adv. Energy Mater.* **2016**, *6*, 1501937.

(80) Burba, C. M.; Frech, R. Vibrational Spectroscopic Investigation of Structurally-Related LiFePO4, NaFePO4, and FePO4 Compounds. *Spectrochim. Acta, Part A* **2006**, *65*, 44−50.

(81) Zhao, S.; Wu, F.; Yang, L.; Gao, L.; Burke, A. F. A Measurement Method for Determination of DC Internal Resistance of Batteries and Supercapacitors. *Electrochem. Commun.* **2010**, *12*, 242−245.

(82) Bai, L.; Gao, L.; Conway, B. E. Problem of in situ real-area determination in evaluation of performance of rough or porous, gas-evolving electrocatalysts. Part 1.-Basis for distinction between capacitance of the double layer and the pseudocapacitance due to adsorbed H in the H2evolution reaction at Pt. *J. Chem. Soc., Faraday Trans.* **1993**, *89*, 235−242.

(83) Burke, A. R&D considerations for the performance and application of electrochemical capacitors. *Electrochim. Acta* **2007**, *53*, 1083−1091.

DOI: 10.1021/acs.jpcc.8b05241
J. Phys. Chem. C 2018, 122, 24499−24511